ACTIVITY MEASUREMENTS OF IMPORTANCE TO STELLAR NUCLEOSYNTHESIS

A Dissertation

Submitted to the Graduate School
of the University of Notre Dame
in Partial Fulfillment of the Requirements
for the Degree of

Doctor of Philosophy

by

Jörn Meißner, M.S., Dipl. Phys.

M. Wiescher, Director

Department of Physics
Notre Dame, Indiana

October 1996

ACITIVTY MEASUREMENTS OF IMPORTANCE TO STELLAR NUCLEOSYNTHESIS

Abstract

by

Jörn Meißner

Remnants of supernovae, especially SN 1987A, are expected to be partially powered by the decay of ^{44}Ti. A recent COMPTEL observation of ^{44}Ti in CAS A sets upper and lower limits on the initially produced amount of ^{44}Ti. In both cases, a tighter constraint on the half-life can considerably decrease uncertainties.

In order to measure the ^{44}Ti half-life, a secondary beam of ^{44}Ti was produced and separated using the A1200 projectile fragment separator at the NSCL at Michigan State University. Several samples were prepared by implanting this beam into Al-foils. The integrated intensity of all fragments was monitored continously with beam monitors. Particle identification in the focal plane allowed the determination of quantities of implanted ^{44}Ti, ^{43}Sc, ^{47}Sc, ^{51}Cr, ^{54}Mn and ^{56}Co. Specific activity measurements on the beam-contaminants allowed verification of the number of implanted ^{44}Ti particles. The specific ^{44}Ti activity, which has been corrected for background, coincidence summing and photon absorption effects, yields a half-life of $t_{1/2} = 39 \pm 4$ yrs. This work presents an independent result, with a very different value compard to most previous measurements. With this new value an initial abundance of ^{44}Ti in CAS A has been calculated: $7{\cdot}10^{-4}$ $M_{\odot}$. Current supernova models predict about one order of magnitude less.

Jörn Meißner

The neutron capture rates on ^{18}O and ^{15}N are of considerable interest in the interpretation of nucleosynthesis in inhomogeneous Big Bang scenarios and for stellar Helium burning in massive Red Giant stars as well as in low mass AGB stars. We measured the reaction cross section of $^{18}O(n,\gamma)^{19}O$ and $^{15}N(n,\gamma)^{16}N$ at the Forschungszentrum Karlsruhe with a fast cyclic neutron activation technique at laboratory neutron energies of 25, 129, 152, 250 and 370 keV. Direct capture and shell model calculations were performed to interpret the results as well as previous unpublished data. For ^{18}O the reaction rate is in good agreement with previous rates for typical He-burning temperatures. The strength of a resonance at 152 keV was overestimated previously, resulting in a smaller reaction rate between 0.5 and 1 GK. The reaction rate for ^{15}N is 30% to 50% smaller than the previously used theoretical rates, mainly due to a change in literature values for spectroscopic factors. Neither reaction rate will significantly alter the previously calculated reaction flow pattern, nor does either reaction act as a neutron poison during the s-process.

TABLE OF CONTENTS

LIST OF FIGURES

LIST OF TABLES

ACKNOWLEDGEMENTS

I would like to thank my advisor Dr. M. Wiescher for the opportunity to work with him. He introduced me to the diversity of the field by inviting me to participate in many projects.

Thanks go to Dr. J. Görres who provided invaluable help during the experiments and in discussions.

My (ex-) fellow graduate students Dr. C. Iliadis, Dr. G. Ross, Dr. K. Scheller, H. Schatz, P. Tischhauser, S. Vouzoukas helped out during many experiments and made life in the NSL more enjoyable.

Thanks go to Dr. H. Herndl for his work on the shell model calculations and for being a friend and nice house mate.

Dr. E. Berners, Dr. L. Lamm, J. Kaiser, C. Guy, A. Hovarth and his crew helped me out whenever I needed them with some hardware or electronics problem.

I would like to thank the TRIUMF/SFU collaboration with Dr. S.M. Graaf, R. Lange, Dr. J. Vincent, Dr. J. d'Auria, Dr. U. Giesen, Dr. L. Buchmann, who provided me with hospitality during my stay in Vancouver and helped me prepare a ^{44}Ti source for my calibrations; my MSU-Collaborators, especially Dr. B. Sherril, Dr. M. Steiner, Dr. D. Bazin for helping me with beam intensity calculations during the analysis and online help during the experiment; and my FZK collaborators F. Käppeler, H. Beer, S. Jaag, E. Ernst and his accelerator crew.

Dr. D.D. Clayton, Dr. R. Hoffman, Dr. R. Diehl, Dr. A. Iyudin, Dr. N. Langer, Dr. S. Shore and Dr. R. Gallino provided me with some insight during

discussions on ^{44}Ti observations and stellar network calculations.

I would like to thank Dr. H.-J. Körner for referring me to Notre Dame initially. Without him, I would never have found out about M. Wieschers' group.

Last but definetively not least I would like to thank my parents for encouraging me to strive for my ideas and to follow through on seeking my goals.

My work was supported in by the National Science Foundation and the Canadian Council for Research and Engineering. In part my work was supported by graduate research grants from the National Academy of Science and the University of Notre Dame Zahm Research Fund.

CHAPTER 1

INTRODUCTION

Nuclear physics is fundamental to our understanding of stellar phenomena. Matter consists of electrons, protons, neutrons and their compounds. The composition of matter, nucleosynthesis, began, when the expansion of the early universe after the Big Bang allowed the matter to cool down sufficiently for protons and neutrons to freeze out and to react with each other. Light elements were produced. If the freeze-out from the quark-gluon plasma was a 1st order phase transistion, zones of high and low baryon density were formed. Because neutrons have a larger mean free path than protons due the charge, neutrons will diffuse into the low-density regions. As a result high density proton rich and low density neutron rich zones form, the basis for inhomogeneous Big Bang models. Nucleosynthesis in a universe that has both neutron and proton rich regions will produce more ^{2}H, less ^{4}He and more ^{7}Li than a homogeneous proton rich universe with the same global value for the baryon density [1]. According to Ref. [1] and references therein, there is consensus in the literature that the these light element abundances cannot be fitted with any inhomogeneous model with a closure density of baryons. This does not necessarily imply that the Big Bang was homogeneous, but it requires $\Omega_b < 1$ [1].

In stars matter is processed mainly from protons into higher atomic masses. While the star is on the main sequence in the Hertzsprung Russel diagram, it mainly burns hydrogen to helium (H-burning) by the so called proton-proton chain and the CNO cycle. As a net result for the p-p chain as well as the

CNO cycle, 4 protons are converted into one ^{4}He releasing about 26 MeV. Some losses in the 2–28% range occur due to escaping neutrinos [2]. Critical for the life of a star is the hydrodynamical equilibrium between gravitational contraction and thermal pressure expansion forces. After the hydrogen fuel is exhausted the hydrodynamical equilibrium is disturbed and the star contracts gravitationally. This adiabatic process increases the temperature and He ignites converting He into ^{12}C by the triple-α process.

Hydrogen abundance X, helium abundance Y, and metallicity Z are defined as mass fractions, adding up to 1 for the star. The metallicity fraction Z includes all elements heavier than helium. It varies several orders of magnitude (10^{-6} — $\approx$ 1), depending on the scenario. The authors of Ref. [3] describe the evolution of a 25 $M_\odot$ star with a He abundance of $Y = 0.28$ and a metallicity of $Z = 0.02$, which illustrates the different burning phases very well: In the initial core hydrogen burning the central temperatures and densities are $T = 37$ MK and $\rho = 3.8$g cm^{-3}. Hydrogen is transformed to helium by the CNO cycle. The main product of the CNO cycle is ^{14}N. This phase lasts for about 6.1 Myr. At H exhaustion temperature and density reach $T = 80$ MK and $\rho = 47$g cm^{-3} due to gravitational contraction. The star is left with a He core of mass $M_\alpha = 6.8 M_\odot$.

He ignition takes place at about $T = 1.4{\cdot}10^8$K and $\rho = 470$g cm^{-3} and He is converted into ^{12}C by the triple-α reaction. When Y_α falls below 0.26, the energy generation drops and the star contracts due to its own gravitation. This triggers the sequence ^{14}N$(\alpha,\gamma)^{18}$F$(\beta\nu)^{18}$O$(\alpha,\gamma)^{22}$Ne(α,n) which produces a high neutron abundance during the last phase of the He-burning, starting the weak component of the s-process ($T = 2.1{\cdot}10^8$K and $\rho = 8{\cdot}10^2$g cm^{-3}) [3]. During the s-process most heavy elements are produced by neutron capture reactions

and β-decays. One distinguishes between the main and the weak component [4]. The weak component produces elements with masses $A < 90$ and may form the seeds for the main component ($A > 90$). At the end of the He core burning the central temperature and density reach $T = 7.5{\cdot}10^8$K and $\rho = 3.3{\cdot}10^3$g cm^{-3}. At this point the star is left with a carbon-oxygen core with a mass $M_{CO} = 6.3M_\odot$ inside a H-exhausted shell $M_\alpha = 8.88M_\odot$. The He burning phase lasts about 0.64 Myr, roughly 10% of the H burning phase. During the whole time neutron densities don't exceed 10^6 n cm^{-3}.

A different scenario of importance to nucleosynthesis of elements with $A > 90$ are low mass stars that have reached the asymptotic giant branch state (AGB stars). Low mass stars ($M < 8 - 10M_\odot$ typically) exhaust their hydrogen fuel at the center much quicker than near the surface due to their higher temperature gradient compared to massive stars. Therefore convection plays a significant role in low mass stars. Typically, AGB stars consist of a CO core with a He shell, surrounded by a H envelope, and have masses ranging from 0.5 to 10 $M_\odot$, whereas their radii might be 5-10 $R_\odot$ [5]. At the interface of the CO core and the He-shell significant amounts of ^{12}C is mixed into the He shell by convection when the star ascends on the first giant branch. This first convective mixing is called the *first dredge up* [6]. Following this the star will continue the He shell burning phase, continuing to contract and heat. Depending on the mass, the star either explosively ignites the He in the core (Core He Flash) or settles down to a quiescent He-core burning phase. After core He exhaustion the star will structurally re-adjust to shell He burning resulting in a strong expansion and a second convective mixing of core and shell material. This *second dregde up* [6] will start the star on its ascend on the asymptotic giant branch. AGB

stars have a high luminosity and are found beyond the red giant stars in the Hertzsprung-Russel (H-R) diagram.

For the production of the bulk of the material in the main component of the s-process the neutrons are provided by several (α,n) reactions, especially on ^{13}C. This source operates in thermal pulses of low-mass AGB stars with low metallicities (see Ref. [4, 7] and references therein). Penetration of the convective envelope in the partially He-burned zone after the quenching of each thermal pulse mixes freshly synthesized ^{12}C, ^{4}He and s-process material into the envelope. This process is called the *third dredge up*. ^{13}C(α,n) is the dominant neutron source in this scenario and is produced by ^{12}C(p,γ)^{13}N($\beta^{+}\nu$)^{13}C [8, 9]. Further mixing from the H-envelope provides more protons into the ^{12}C rich intershell layers for building ^{13}C pockets. Since neutron production by ^{22}Ne(α,n) is negligible in this scenario one has to rely on the ^{13}C(α,n)^{16}O neutron source. Any strong neutron capture reaction on present material may have a severe effect on the s-process nucleosynthesis.

In low mass stars the production of ^{19}F is possible via the reaction sequence ^{18}O(p,α)^{15}N(α,γ). Changing relative abundances of ^{18}O and ^{15}N might have a significant effect on the ^{19}F production. A detailed discussion of ^{18}O and ^{15}N production and depletion mechanisms as well as the importance of both isotopes for the ^{19}F production during the s-process will be given in chapter 3. In the present work we will study neutron capture cross sections of ^{15}N and ^{18}O by a fast cyclic activation method and will discuss the changes on stellar reaction rates due to our results.

Supernova

Supernovae are divided by astrophysicists into two major classes, type I and II. Type I (SNI) are high in heavy elements (oxygen to iron) and very low in hydrogen [2]. Type II supernovae (SNII) contain some heavy elements but are primarily composed of hydrogen.

Massive stars with low metallicities are the typical SNII progenitors. Depending on its mass SNII leave either neutron stars or black holes as remnants. About 20% of the SNII remnants contain a neutron star in the form of a pulsar (see Ref. [2] and references therein). Stars with main sequence masses $M > 8M_{\odot}$ produce a collapsing Fe-core after the end of their hydrostatic evolution (fuel exhaustion). The Fe-core results either from hydrostatic Si burning or C-, O-, and Si-burning in the collapse of a degenerate NeOMg-core.

Due to fuel exhaustion the temperature and pressure drop resulting in material from the shell falling onto the neutron star. This material will bounce back and create the shock front of an explosion. The bounce cannot account for the shock front velocity correctly and the front stalls in this simple approximation. Neutrino winds, releasing the gravitational binding energies of the (proto-)neutron star, might be responsible for driving the shock front in addition to the bounce. The exact trigger mechanism for an explosion after the core collapse is still very much debated. According to Ref. [10] the ignition of supernovae is one of the most serious uncertainties and the least explored aspect of thermonuclear models. Most models are concerned with the burning process, fuel consumption and energy release after the initial ignition. These models deal with the basic question of how the burning front moves and how new nuclear fuel is ignited.

Detonation models are based on a shock driven burning front. New fuel is

heated by shock compression and ignited. Typically the front velocity is supersonic. While the shock front velocity is well understood, models differ by their treatment of the width of the shock and reaction zone. One-dimensional models seem oversimplified [10]. If the scale of the turbulence is larger than the width of the burning front it wrinkles which results in an increase in surface area and in the velocity of the front. These wrinkles exhibit significant 3-dimensional structure. Cellular or spinning detonations [11] might cause an increase in surface area and therefore increased yields during nucleosynthesis.

SNI are binary systems containing CO white dwarfs accreting matter from a companion star onto an accretion disk. Matter is processed in the accretion disk by H- and He-burning to carbon and oxygen and thereby increasing the mass of the CO-core. Eventually the core exceeds the Chandresekar mass and collapses. The explosion continues mostly as a deflagration and sometimes as a detonation.

Deflagration models assume convective burning. The hot ashes of the burning front mix with cold fuel and heat it to ignition. The propagation velocity depends on the heat transfer and is always subsonic. Nomoto *et al* [12] suggested that the burning front is propagated by turbulent convection rather than by heat diffusion only. If the scale of the turbulence is small compared to the width of the burning front the deflagration stays laminar. This type of burning can be studied using one-dimensional models. If, however, the scale of the turbulence is larger than the width of the burning front, 2 or 3 dimensinal calculations will yield a factor of 2-3 more Ti than one dimensional models [10, 13]. Figure 1.1 shows the contours of energy generation rate at two constant times for a two dimensional hydrodynamic computation by Ref. [14]. The initial state was a spherical burning front with 1% pertubations in the velocities to break the sym-

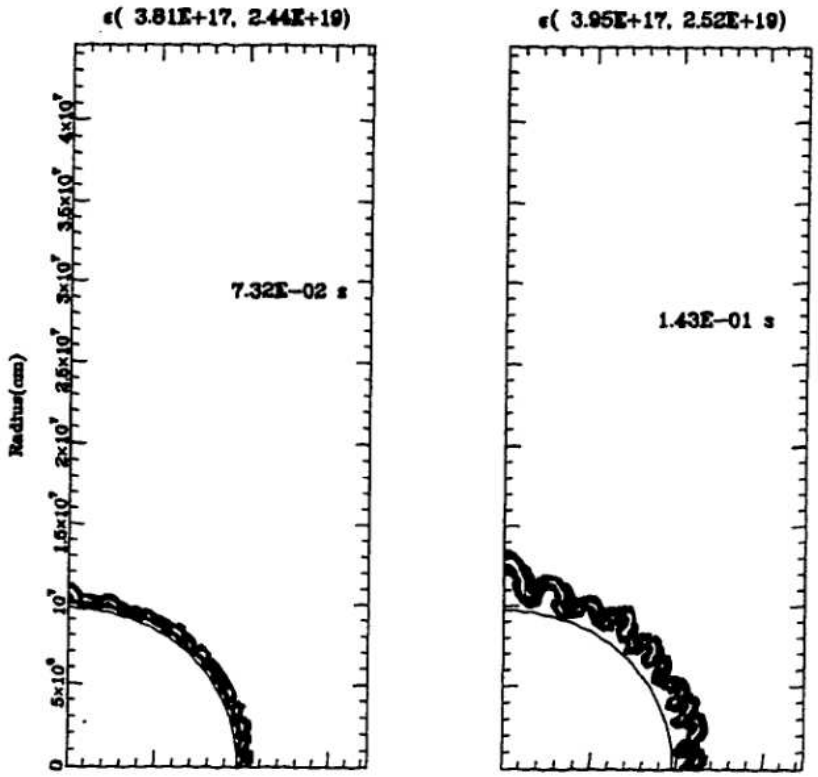

Figure 1.1: Deflagration front from a 2-dim hydrodynamics calculation (from Ref. [10]).

metry. The development of a wrinkled structure is clearly visible. In Ref. [14] the authors compare the 2D calculation with the 1D equivalent. The enhanced flame area results in a higher rate of fuel depletion and a reduction of electron capture rates due to the faster expansion.

This approach still causes problems [10] in new models (e.g. Ref. [15]) since they don't reproduce the front velocity correctly. At small length scales, 3-dimensional models might clarify the physical nature of the process and suggest what "subgrid" size and velocity should be used [10].

In models for both, SNI and SNII, ^{44}Ti is produced during the α-rich freezout

from the nuclear statistical equilibrium (NSE) in the Si burning stage. Differences in 1D and multi dimensional models change the amount of produced ^{44}Ti significantly. Some additional ^{44}Ti can also be produced during other burning phases, for instance in the outer layers during explosive hydrogen burning. The production mechanism and the importance of ^{44}Ti in these models is described in chapter 2. It is followed by a discussion of the ^{44}Ti half-life and its importance for the comparison of models and observational data.

CHAPTER 2

THE ^{44}Ti HALF-LIFE

2.1 Motivation

When temperatures in supernovae reach 3-4 GK nuclei are synthesized and destroyed by capture reactions and photodisintegrations in a complete equilibrium. The abundances depend only on the binding energies (B, nuclear masses), density and temperature. This is commonly called nuclear statistical equilibrium (NSE) [16]. Since the energy distribution of all nuclei can be described by a Maxwell-Boltzmann distribution, the abundance of each nucleus, $Y(Z,N)$, depends strongly on $\exp(-B/kT)$. We expect a nuclear distribution around ^{56}Fe, where we find the highest binding energies [16]. Binding energies for nuclei exhibiting an α-cluster structure are typically high. ^{44}Ti is one such nucleus with a high binding energy. Therefore, it is thought to be produced mainly during the α-rich freezeout from NSE [17] during the Si-burning stage in supernovae. The α-rich freezeout occurs while the burning process is still at equilibrium: the temperature and density drop significantly because of the decompression following the shock or deflagration front passage. During the rapid cooling free α particles do not have enough time to merge back into the Fe region by the triple-α-reaction (see Ref. [18] and references therein).

The production of ^{44}Ti is model-dependent. However, there seems to be a general consensus among one dimensional models for a given type of supernova. Mahoney *et al* [19] discuss this in more detail: for SNs Ia, carbon deflagration

models of accreting carbon/oxygen white dwarfs yield (0.2-0.8)·$10^{-4} M_{\odot}$ of ^{44}Ti [20, 21], whereas helium detonation models of accreting carbon/oxygen white dwarfs [22] yield (0.2-4.5)·$10^{-4} M_{\odot}$.

An exception to this is described by Woosley and Weaver [23]: In sub-Chandrasekhar mass models for SNIa, where the He-detonation in the accreting disk ignites the CO-core of the white dwarf, ^{44}Ti is overproduced. With masses between 0.6 and 0.9 $M_{\odot}$ for the CO white dwarf and accretion rates of several times 10^{-8} $M_{\odot}$, quantities of ^{44}Ti were produced between $2.1 \cdot 10^{-4}$ and $39 \cdot 10^{-4}$ $M_{\odot}$. Note, that in this scenario the material never achieves NSE and is therefore not really an α-rich freezeout.

Type II supernova models give a ^{44}Ti yield of about (0.5-2)·$10^{-4} M_{\odot}$ [17, 24, 25]. It is argued by the authors of Ref. [19, 26] that the yield in SNs Ib is comparable to the production in SNs Ia.

Two dimensional supernova models, as discussed in the introduction, have an increased area of the burning front. The resulting production of ^{44}Ti might therefore be considerably enhanced. Woosley [13] suggested enhancements of about a factor of 2 compared to one-dimensional models.

Large quantities of ^{44}Ti cannot be ejected unless large quantities of ^{56}Ni are also ejected [27] (excluding the 0.6-0.9 $M_{\odot}$ CO white dwarf models discussed in Ref. [23], where ^{44}Ti is overproduced with respect to ^{56}Fe). ^{56}Ni ($t_{1/2}$=6.1d) decays to ^{56}Co ($t_{1/2}$=77.3d) which in turn decays by electron capture and β^{+} to ^{56}Fe. The latter decay contributes significantly to the light curve of the supernova due to the annihilation radiation. Presence of the ^{56}Co in γ-ray spectra of the remnant or in the light curve might suggest that a significant amount of ^{44}Ti was also produced. The light curve is then expected to be powered by the

^{44}Ti(EC)^{44}Sc(β^+,EC)^{44}Ca decay, after ^{56}Co and ^{57}Co have sufficiently decayed. SN1987A is a good candidate for this behavior [25]. After about 2000 days the ^{44}Ti decay is expected to power the light curve of this remnant [25]. To study the light curve and fit the initial amount of ^{44}Ti a tighter constraint on the half-life is necessary.

The supernova Cas A is generally believed to be Type Ib with a massive Wolf-Rayet star as a progenitor (Ref. [28, 29] and references therein). For the first time γ-ray fluxes from the ^{44}Ti-decay originating in a SN remnant (Cas A in this case) have been observed [28]. Iyudin *et al* [28] measured the γ-ray flux of the 1157 keV γ-ray line from the ^{44}Ti decay in Cas A to be $F_\gamma = (7.0 \pm 2.1) \cdot 10^{-5}\gamma\mathrm{cm}^{-2}\mathrm{s}^{-1}$, which is marginally consistent with the upper limit from an OSSE observation, $F_\gamma < 5.5 \cdot 10^{-5}\gamma\mathrm{cm}^{-2}\mathrm{s}^{-1}$ [30]. Figure 2.1 shows a likelihood map for the origin of 1157 keV γ-ray observed by COMPTEL. The abscissa and ordinate show galactic longitude and latitude in degrees, respectively. The white cross indicates the position of supernova remnant Cas A in nice agreement with the highest likelihood for the origin of the 1157 keV γ-ray. More recent results of the COMPTEL group indicate a lower flux for the 1157 keV emission. The current flux value is $F_\gamma = (4.2 \pm 0.9) \cdot 10^{-5}\gamma cm^{-2}s^{-1}$ [31, 32]. The flux value and the half-life are closely related to the determination of the ejected ^{44}Ti mass. Figure 2.2 gives an overview on the expected masses of ^{44}Ti for different life-times and ages of CAS A.

The date of the event is somewhat uncertain. It ranges from 1658±3 AD [33] to 1680 [34], representing an age range of 312-338 years at the time of observation. Ashworth [34] argues that a "proper motion study" by the authors of Ref. [35], which yields 1667±8 as the date of the event, is consistent with

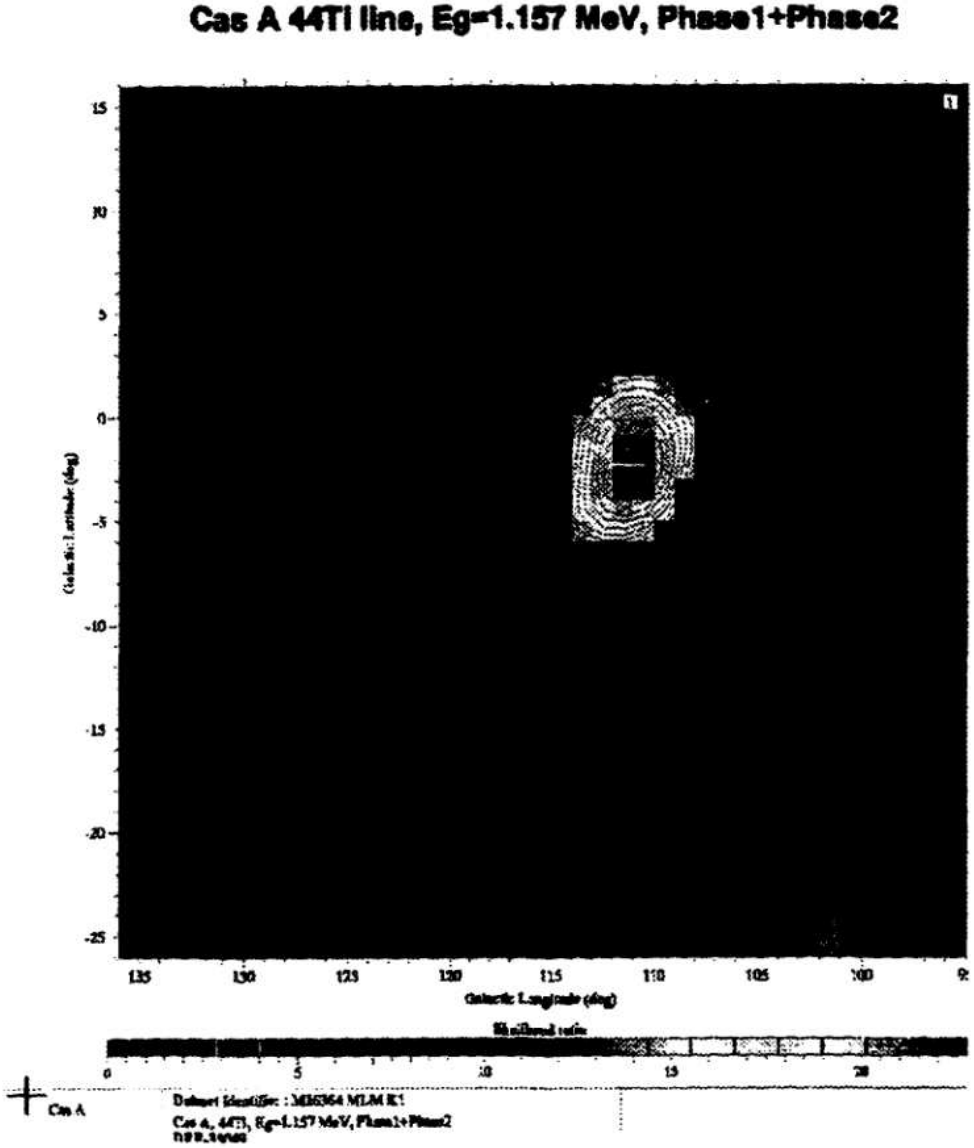

Figure 2.1: Likelihood map for the origin of the 1157 keV γ-ray emission observed by COMPTEL. The position of supernova remnant CAS A is indicated by a white cross. Courtesy of A. Iyudin, MPE, Garching.

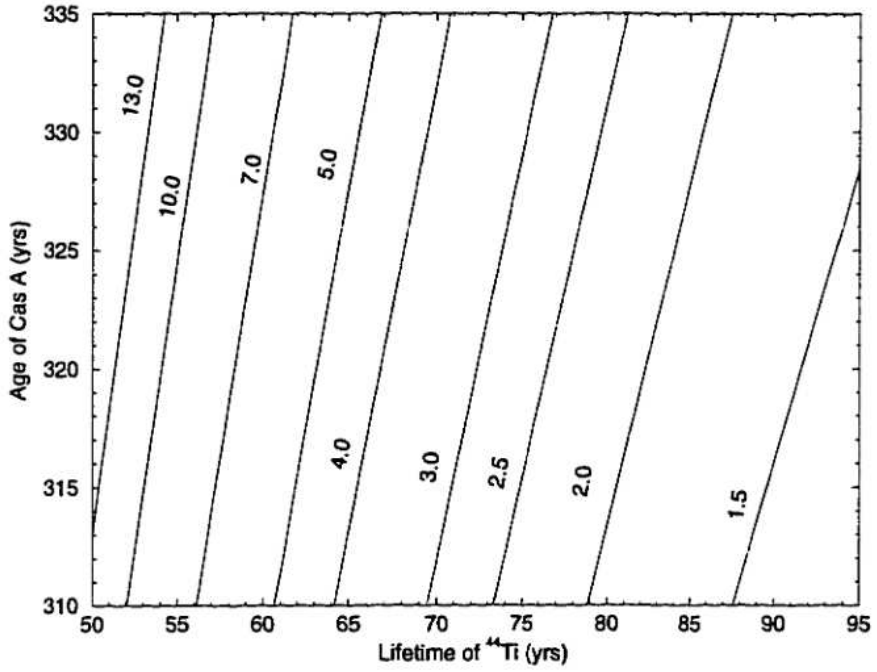

Figure 2.2: Overview on ^{44}Ti yield in units of $10^{-4}M_{\odot}$ in supernova Cas A. Calculations have been performed for $F_{\gamma} = 4.2{\cdot}10^{-5}\,\gamma cm^{-2}s^{-1}$ and $D = 2.92$kpc.

the observation by Flamsteed [36]. The inconsistences in the exact position within 12' of Flamsteed's observation and 3 Cassiopeiae could be attributed to an unlikely but not unprecedented error by Flamsteed. For a detailed discussion see Ref. [27, 34]. In agreement with Ref. [27, 34, 37] we accept the later date, AD1680 and therefore an age range of 312—313 years, depending of the observation period of COMPTEL.

In order to extract the amount of initially produced ^{44}Ti from the γ-ray flux, certain parameters play an important role. The flux is measured only in a small solid angle. The distance to CAS A enters quadratically into our analysis. The life-time τ enters as

$$\tau \exp(t/\tau), \tag{2.1}$$

where t is the age. Section 2.4 discusses the equations in more detail. With this

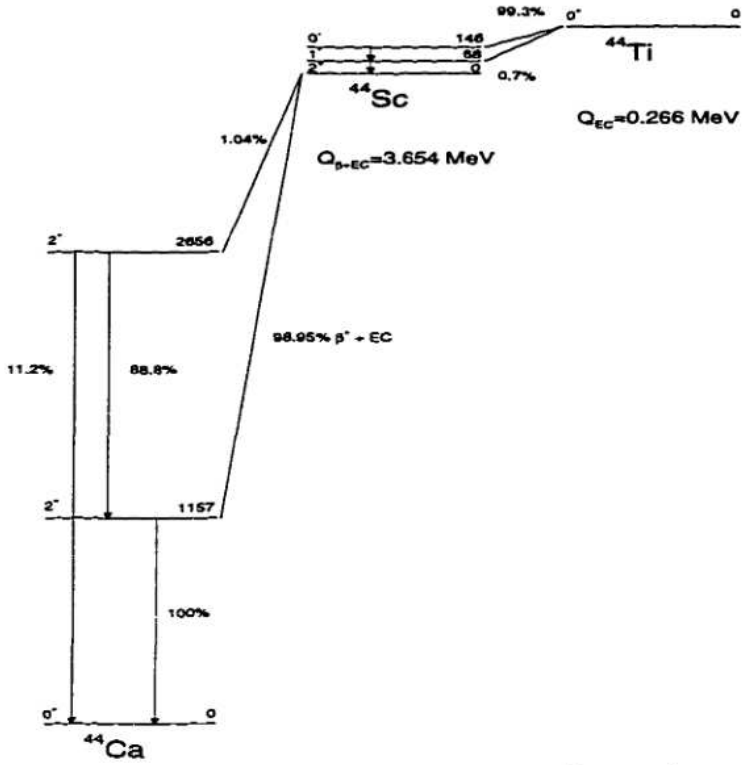

Figure 2.3: Simplified decay scheme of ^{44}Ti(EC).

τ dependence it easy to see that a tighter constraint on the ^{44}Ti half-life would provide a rare opportunity to calibrate current type Ib supernova models.

2.2 The ^{44}Ti decay and previous experiments

Figure 2.3 shows a simplified decay scheme for ^{44}Ti and its subsequent daughter decays. ^{44}Ti decays by electron capture (EC) to the 146 keV state in ^{44}Sc. This state decays by a 2-γ cascade (68 and 78 keV) to the ground state. ^{44}Sc decays by EC and β^+ to excited states in ^{44}Ca. In 99.9% a 1157 keV gamma ray is emitted. Once the ^{44}Ti decay is in equilibrium with the ^{44}Sc decay ($>$ 12 hrs, $\approx$ 3 ^{44}Sc half-lifes), the emission rates for 68, 78 and 1157 keV γ-rays are the same.

Several half-life measurements preceeded the present study. Figure 2.4 gives

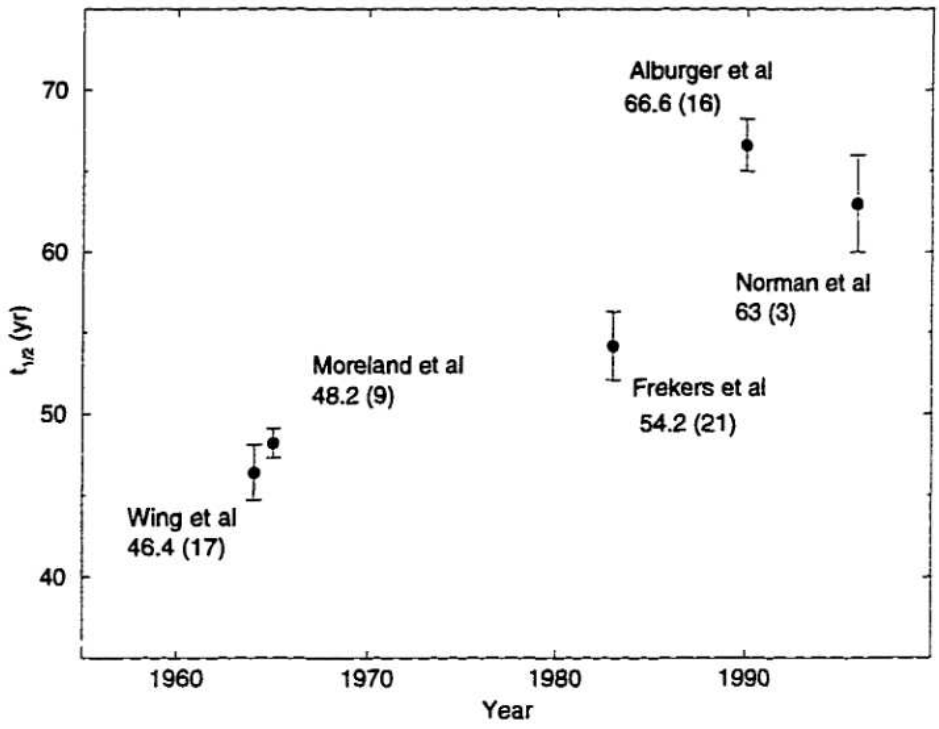

Figure 2.4: Previous results from ^{44}Ti half-life measurements.

and overview on the measured half-lifes. Wing *et al* [38] determined the half-life by measuring the specific activity of isotopically diluted samples. The ^{44}Ti was produced by bombarding scandium oxide with 21 MeV deuterons at the Argonne 60-inch cyclotron. The only stable scandium isotope is ^{45}Sc. While ^{44}Ti was produced by the ^{45}Sc(d,3n) reaction, significant amounts of ^{46}Sc were also produced, possibly by capture of thermalized neutrons on ^{45}Sc ($\sigma_{th} = 27.2 \pm 0.2$ b [39]). ^{46}Sc decays to ^{46}Ti which cannot be separated chemically from ^{44}Ti. The activity measurement was performed with NaI(Tl) scintillating detectors. Coincidences between the two annihilation γ-rays were measured with two 2.5" by 2.5" NaI detectors coupled to single channel analysers while the 1157 keV activity was measured with 3" by 3" NaI detector coupled to a 256 channel analyser. The efficiency calibration of the NaI detectors was done at 511 keV

and 1275 keV (^{22}Na source). No details are given for correcting the efficiency to 1157 keV, the ^{44}Ti γ-ray energy. No reference was made to the different β^+ energies of ^{22}Na and ^{44}Ti (0.544 MeV and 1.467 MeV, respectively), which could significantly influence the range of the positrons. This would affect the position of the annihilation radiation origin and therefore possibly the efficiency of the coincidence setup. For details on the method of measuring the isotopic ratios of the individual samples by mass spectroscopy, Wing *et al* refer to Moreland and Heymann [40].

Moreland and Heymann [40] also used mass spectroscopy of isotopic diluted ^{44}Ti solutions to determine the amount of present ^{44}Ti. Their ^{44}Ti was produced via ^{45}Sc(p,2n) by bombarding a scandium foil with 22 MeV protons at Oak Ridge National Laboratory. Again, significant amounts of ^{46}Ti were produced, possibly by neutron capture of neutrons from the (p,2n) reaction that produces ^{44}Ti [1]. Moreland and Heymann [40] determined the γ-activity in a similar setup as in Ref. [38], but they accounted for different positron ranges for ^{22}Na and ^{44}Ti, reducing a systematic uncertainty between 3.3-5% to 1.8% [40]. The critical issue in both papers is the determination of the absolute number of ^{44}Ti particles by mass spectroscopy. The samples were spiked with a Ti solution, enriched in ^{46}Ti. The ratio ^{46}Ti/^{48}Ti of the spike-solution was analysed in the Argonne 100 inch, double focusing mass spectrometer and in two "conventional" 12 inch mass spectrometers. Results for this ratio were quoted with 4% uncertainty, which the authors propagated as a statistical uncertainty, rather than a systematic one. Analysing several spiked ^{44}Ti solutions in the Argonne 100" mass spectrometer,

[1] During our irradiation of Sc-metall at TRIUMF in order to produce a calibration source for the γ-ray efficiency, significant amounts of ^{46}Sc were observed. ^{46}Sc was one of the most prominent contaminants.

the ratios

$$\frac{^{44}\mathrm{Ti}}{^{46}\mathrm{Ti}_{total}} \tag{2.2}$$

and

$$\frac{^{46}\mathrm{Ti}_{total}}{^{48}\mathrm{Ti}} = x \tag{2.3}$$

were determined. Here $^{46}\mathrm{Ti}_{total} = {}^{46}\mathrm{Ti}_{nat} + {}^{46}\mathrm{Ti}_{spike}$. From this and the natural ratio

$$\frac{^{46}\mathrm{Ti}_{nat}}{^{48}\mathrm{Ti}_{nat}} = y, \tag{2.4}$$

the absolute amount of $^{46}\mathrm{Ti}_{nat}$ could be calculated:

$$^{46}\mathrm{Ti}_{nat} = \frac{^{46}\mathrm{Ti}_{spike}}{x}\frac{xy}{x-y}. \tag{2.5}$$

This absolute number together with the ratios yielded the total number of ^{44}Ti. It should be noted that the "natural" ratio $^{46}\mathrm{Ti}/^{48}\mathrm{Ti}$ could be significantly changed due to production of ^{46}Sc during the ^{45}Sc irradiation (see Ref. [41, 42]). These possible changes have not been investigated in these experiments. It is furthermore essential for this chemical method that no material adsorbs to the hardware when solutions are transferred into different vials or into the ion source. Within an uncertainty of 5% all material has been accounted for after such transfers. Again, this uncertainty was propagated as statistical and not as a systematic uncertainty. Therefore the result for the half-life of Ref. [40] and Ref. [38] should be associated with an additional 9% of systematic uncertainty, which has to be added linearly rather than quadratic to the averaged result for the half-life.

Frekers *et al* [42] also produced a ^{44}Ti sample using the ^{45}Sc(p,2n)^{44}Ti reaction. Accelerator mass spectroscopy (AMS) with the Argonne Enge split-pole magnetic spectrograph was used to determine the isotope ratios $^{44}\mathrm{Ti}/\mathrm{Ti}$. The

specific activity was measured with a high resolution Ge(Li) detector at a distance of 100cm. In contrast to mass spectroscopy, where electrostatically (10-40 keV) accelerated ions are directly analysed with a magnetic spectrometer, AMS requires a completely different setup. In this experiment negative ions of Ti-compounds were generated in a Cs-sputter ion source. The desired mass was selected by sweeping the field of a 40° inflection magnet. Ions were accelerated with the Argonne FN tandem Van-de-Graaff accelerator. In the terminal of the accelerator electrons were stripped off the ions with a carbon foil. Molecular ions break up into atomic ions. The distribution of charge states after stripping plays an important role in AMS and will be discussed further below. The accelerated beam is transported by magnetic focusing and bending elements only to the Enge split-pole magnetic spectrograph. Once the magnetic rigidity of the beam transport system is set, the rigidity of the ions is only changed by adjusting the terminal voltage of the accelerator. A second stripper foil is located in the scattering chamber of the split-pole magnet. This is necessary for further reduction of beam contaminants, as discussed below. Ref. [42] discusses a number of possible experimental error sources, some of which I would like to point out here:

- The charge state distribution is velocity dependent. Distributions for different charge states of the same ion usually overlap. Attention has to be paid to the charge state selection, so that small terminal voltage changes do not affect the fraction of the selected charge state versus others. (e.g. one should stay on the "plateau" of the distribution rather than on the steeper slopes). This is especially important when comparing two different ions, since changes of the terminal voltage might have different effects on

the respective charge state distributions.

- Ion optical focusing effects of the acceleration tubes change with the terminal voltage. This affects the transmission of ions.

- To control the voltage on the terminal a slit feed back system can not be used due to almost vanishing currents (pA range). Instead the voltage is controlled by a generating voltmeter. Frekers *et al* show that a variation in terminal voltage causing a ± 15 keV change at 8.2 MV can alter the rigidity of the ions enough to change the resulting mass fractions by a factor of two.

- Many ions are injected into the accelerator as negatively charged molecules. They fit the mass requirment by the inflection magnet, ± 2 a.m.u. A wide variety of charge states and ions are now possible yielding an almost "white" energy spectrum after acceleration. Since only p/q is selected a large portion of these unwanted ions will be transported to the spectrograph, where they create a huge background. Additional strippers are necessary to select only one charge state. All beam contaminants have to be known in order to analyse isotopic ratios.

All these systematic error sources were investigated by Frekers *et al.* Were appropriate, corrections were applied or errors estimated. As can be seen, AMS experiments require a lot of attention to several parameters that could easily result in systematic uncertainties.

Alburger and Harbottle [43] measured the ^{44}Ti decay curve relative to ^{36}Cl with a gas-flow proportional counter. They used two independently produced

samples. One was made from a solution used by Frekers *et al* [42]; the second was from unknown origin. Since this method is not dependent on the knowledge of the absolute number of ^{44}Ti in the samples, Alburger and Harbottle [43] present an independent method to the previous experiments. At first sight it seems that a decay curve measurement is straight forward and leaves little room for systematic uncertainties. Measuring the ^{44}Ti activity relative to a ^{36}Cl source reduces uncertainties related to possibly changing gas pressures, amplifier gain, and detector bias. The largest disadvantage of this setup is that no energy discrimination is possible. The gas counter only detects charged particles, namely β^- and β^+ particles for ^{36}Cl and ^{44}Ti, respectively. Source contaminations with β-emitting isotopes of a longer half-life could flaten the decay curve. Alburger and Harbottle investigated possible contaminants of either sample and determined that none could be found in high resolution γ-spectra below 3 MeV. The β-spectra of the sample were measured with a plastic scintillator. They showed the expected endpoint at 1476 keV. The analysis of the shape is not explained in detail. Without a precise study of the β-spectrum's shape β-emitters with a lower endpoint energy and intensity might remain hidden. β-emitting isotopes with half-lives between 40 and 500 years are listed in Tab. 2.1. The respective endpoint energy is less than 1.47 keV in all cases, fitting the criteria for possible contaminations. However, production of these isotopes is difficult to explain without any information on the materials used during the ^{44}Ti production. In order to roughly estimate possible contributions we will refer to the ^{45}Sc irradiation we performed at TRIUMF in order to produce a γ-ray calibration source:

Impurities in the Sc metal include Mg, Al, Si, Ti, Mn, Fe and Ni as well as some rare earth metals, all at the ppm level for 99.9% pure Sc powder [44].

Not all elements are tested in a typical lot analysis. Therefore only estimates can be made for other contaminations. During an irradiation with 20-60 MeV protons, significant amounts of neutrons are produced [41, 45]. Our sample was imersed in water for cooling. Besides the cooling effect water also thermalizes neutrons. This opens up the possiblility for thermal neutron capture. From γ-activity measurements we obtained the ratio of ^{46}Sc to ^{44}Ti in our activated sample. With cross sections for the (p,2n) reaction between 30 mb [45] and 70 mb [41] and 27 b for thermal neutron capture on ^{45}Sc [39] we calculate the ratio of thermal neutrons to incident protons $8{\cdot}10^{-4} < N_n/N_p < 2{\cdot}10^{-3}$. With a total proton exposure of about 1500 μAh this yields a total thermal neutron exposure of $2.7{\cdot}10^{16} < N_n < 6.0{\cdot}10^{16}$. With the assumption that ^{46}Sc is only produced by thermal neutrons the yield of several isotopes can be estimated relative to ^{46}Sc. Table 2.1 lists β-emitting isotopes with half-lives between 40 and 500 years. Out of all of these isotopes only ^{62}Ni and ^{150}Sm have a significant thermal neutron capture cross section. If these are present in natural abundance at the 2 ppm level an activity of $5.9{\cdot}10^{-3}$ and $6.55{\cdot}10^{5}$ (18μCi) could be produced for ^{63}Ni and ^{151}Sm, respectively. It should be noted that the activity of ^{151}Sm is even larger than the initial ^{44}Ti activity of the irradiated material (15μCi), whereas Ni can be neglected. Since ^{151}Sm emits a γ-ray at 22 keV only, it is possible that Alburger and Harbottle would not have seen this isotope in their γ-ray spectra due to photon absorption effects in the detector window. A double neutron capture on ^{30}Si is rather unlikely to produce significant amounts of ^{32}Si, especially in light of the small cross sections ($\sigma_{th} \approx 0.1$b in both cases). ^{158}Tb could be produced by the ^{159}Tb(p,d) reaction. This analysis has to be taken with several grains of salt: First, the impurities given in the specification sheet are usually upper limits;

TABLE 2.1: β-EMITTING ISOTOPES WITH 40yr $\leq t_{1/2} \leq$ 500yr

Isotope	$t_{1/2}$ (yr)	Radiation Type	$\sigma_{n,\gamma}$ (barn)	Yield [a]	Activity (1/s)
^{32}Si	172	β^- 0.2 MeV, no γ	[b]		
^{39}Ar	269	β^- 0.6 MeV, no γ	0.8	$25{\cdot}10^{3}$	
^{63}Ni	100	β^- 0.1 MeV, no γ	14.5	$27{\cdot}10^{6}$	$5.9{\cdot}10^{-3}$
^{121}Sn	55	β^- 0.4 MeV, γ 37	0.14	$2.4{\cdot}10^{6}$	$9.4{\cdot}10^{-4}$
^{151}Sm	90	β^- 0.1 MeV, γ 22	104	$2.7{\cdot}10^{15}$	$655{\cdot}10^{3}$
^{158}Tb	180	β^- 0.9 MeV, γ 944	[c]		

[a]calulated for the sample irradiated at TRIUMF under the conditions described in the text.

[b]double neutron capture necessary

[c]no neutron capture, but (p,d) reaction possible

second, our ^{44}Ti source was produced from an entirely different Sc stock than in the previous experiments; third, the solution of the irradiated material went through a chemical cleanup procedure that might have eliminated the discussed contaminants.

It is difficult to imagine that a significant contamination of their ^{44}Ti solution would have been unnoticed by the experimenters. With a half-life of $t_{1/2} = 66.6 \pm 1.6$ Alburger and Harbottle have a significantly higher value than all previous measurements (see Fig. 2.4).

Norman *et al*[46] measured the decay curve of ^{44}Ti with a high resolution Ge-detector. ^{44}Ti was produced by the ^{45}Sc(p,2n)^{44}Ti reaction with 40 MeV protons [41, 45] and chemically separated from most other elements. Approximately 0.01 μCi were mixed with 0.04 μCi of ^{22}Na and 0.05μCi of ^{137}Cs, dried and sealed. The activity of this sample was measured together with an ^{241}Am source with a HPGe detector in 24-hour intervals. After 2 years counting the decay curves were evaluated. The half-lives of ^{241}Am and ^{137}Cs could not be reproduced. The ^{22}Na

half-life agreed within 0.5% with the known value. A small ^{54}Mn contaminant in the source also yielded the correct half-life within 1%. The ^{44}Ti half-live was therefore determined relative to the ^{22}Na decay curve yielding $t_{1/2} = 63 \pm 3$ years. The decay curve determined from the low energy lines in the ^{44}Ti decay, however, yielded values of around 46 years [47]. While ^{22}Na γ-ray energy is relatively close to the ^{44}Ti γ-ray energy at 1157 keV, the ^{241}Am and ^{137}Cs are significantly lower (300 – 662 keV). The authors assume that the γ-ray efficiency might change over time. No consistent result was obtained from all decay lines of ^{44}Ti, nor from other sources except ^{22}Na The authors started a measurement to re-investigate the low energy lines in ^{44}Ti at 68 and 78 keV.

Clearly the measured values for the ^{44}Ti half-life span a wide range. The mass spectroscopy and AMS measurements are in good agreement with each other, whereas the decay curve measurements seem to predict significantly higher values. Judging from the astrophysical importance of a tighter constraint on the ^{44}Ti half-life, more measurements are desirable. In the present work we will present a new method to determine the ^{44}Ti half-life.

2.3 Experimental Method

In the present study we have employed a completely different approach to produce and implant an accurately determined number $N_{impl.}$ of ^{44}Ti atoms into a sample. The specific γ-activity A of the sample was then determined during an off line measurement with a germanium detector. The half-life $t_{1/2}$ can be determined then from the differential decay law,

$$\frac{dN}{dt} = -\lambda N, \tag{2.6}$$

with $\lambda = \ln(2)/t_{1/2}$ as the decay constant. Since the time of implantation stop is not coincident with the activity measurement, Eq. 2.6 had to be corrected for the waiting time t_W between the implantation stop and an appropriate time $\bar{t}$ of the activity measurement by a factor $\exp(-\lambda t_W)$. The averaged time $\bar{t}$ should be chosen so that $A(\bar{t})$ reflects the actual activity resulting out of a long measurement. Since the half-life is expected to be long compared to the activity measurement, it is appropriate to choose $\bar{t}$ to be the middle of the measurement. The resulting equation can be solved numerically for the halflife $t_{1/2}$:

$$A(t_W) = -\frac{dN}{dt}(t_W) = \exp\left(-\frac{\ln 2}{t_{1/2}} t_W\right) \cdot \frac{\ln 2}{t_{1/2}} N_{impl.} \qquad (2.7)$$

To verify the feasibility of this method we studied the well-known decay of ^{43}Sc in the same implantation setup. Consistency checks were performed with several other isotopes with half-lives ranging from 36 hours to 312 days. Note that for all calculation one year equals 365.25 days.

2.3.1 ^{44}Ti Production

The production of a suitable ^{44}Ti sample was carried out at the National Superconducting Cyclotron Laboratory at Michigan State University. The goal was to implant a well determined number of ^{44}Ti particles into several samples and reduce the implantation of other isotopes as much as possible. With a primary $^{58}Ni^{15+}$ beam of E/A= 70.6 MeV/u and an intensity of about 20 nA from the K1200 Cyclotron a fragmented beam was produced on a ^{9}Be target (141mg/cm^2). Calculations with the computer code LISE (Ref. [48] and Appendix) predicted the best yield of ^{44}Ti with this target and primary beam combination. Using the A1200 projectile fragment separator (before the upgrade in

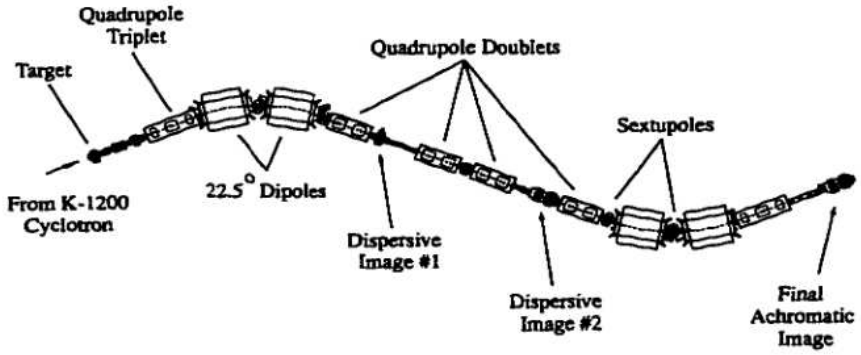

Figure 2.5: Schematics of the A1200 Mass separator at MSU [49]

1994) ^{44}Ti particles were separated from most other fragments. Fragments are selected by the magnetic rigidity,

$$B\rho = \frac{p}{q}, \tag{2.8}$$

where p is the particle momentum and q its charge. B is the magnetic field and ρ the radius of the trajectory, which is fixed by the setup. The A1200's main features are two sets of 22.5° magnetic dipoles for $B\rho$ selection and several dispersive images (see Fig. 2.5). The dispersive images resolve particles with different $B\rho$ to different positions on a plane perpendicular to the beam. At dispersive image #2 an aluminum degrader wedge was inserted (130 mg/cm^2). This wedge causes ions of different nuclear charge Z and different energies to loose momentum and possibly pick up an electron. As a result the magnetic rigidities $B\rho$ of the ions change and the momenta disperse over a wider range. The second set of dipoles is used to narrow down the number of selected ions.

It was originally planned to further reduce beam contaminant in the "Recoil Projectile Mass Separator" (RPMS). The RPMS is essentially a Wien velocity filter combined with a dipole magnet. A Wien filter consists of homogeneous

electric and magnetic fields. The fields are perpendicular to each other and to the beam direction. For straight trajectories through the filter the forces $F_e = qU$ and $F_m = qvB$ for the electric and magnetic field, respectively, have to cancel out. Therefore only for velocities $v = U/B$ will ions travel on a straight line throught the filter.

Unfortunately, it was discovered during the experiment that the RPMS was misaligned with the A1200 and the transmission of the fragmented beam to the RPMS was several orders of magnitudes less than expected. A new setup had to be improvised, avoiding the missaligned beamline between the A1200 and the RPMS. The implantation and particle counting was moved to take place in the focal plane of the A1200 (final achromatic image in Fig. 2.5). The time constraints only allowed a simple setup: A plastic scintillator (T0) was installed on an actuator. It could be inserted into and removed from the focal plane remotely. A second remote controlled actuator sat opposite of the T0-detector in the focal plane. Only one actuator could be inserted at a time due to space constraints. The second actuator was used to either insert our sample or a 500μm Si PIN diode (ΔE detector). To reload this actuator the focal plane chamber had to be opened to air. We installed the PIN diode before and after each implantation run. Both, T0 and ΔE detector, had an area of 5cm by 5cm.

Three samples were prepared. Each sample consisted of a stack of aluminum foils: A 500μm thick absorber foil, to slow down the ^{44}Ti ions, a 400μm to 460μm thick sample foil to hold the implanted ions, and a 150μm to 250μm thick veto foil. The fragmented beam was implanted into the respective sample stack for 5.5, 7.5 and 7.0 hours.

Range calculations were performed with the computer code LISE [48] and

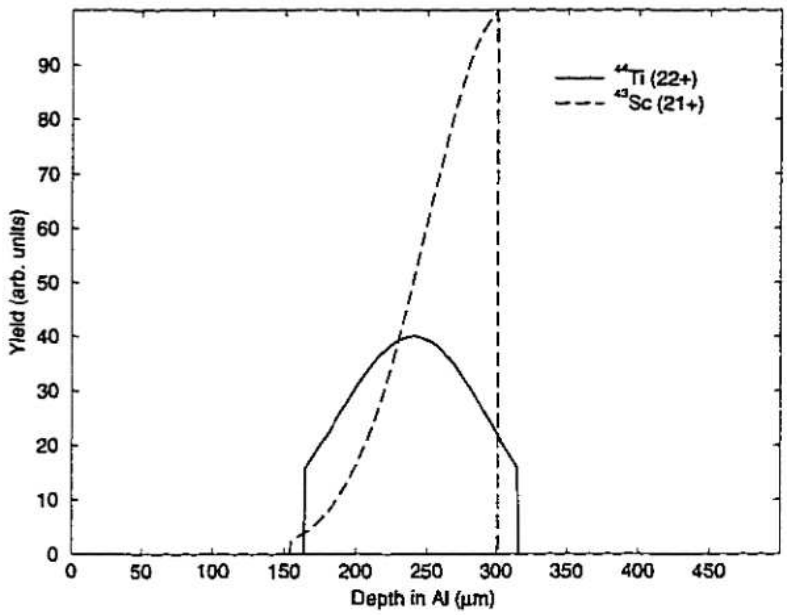

Figure 2.6: Range distribution of ^{44}Ti and ^{43}Sc in the sample foil based on the momentum distribution on the focal plane.

INTENSITY[50]. A description of these programs can be found in the Appendix. With the A1200 optimized for ^{44}Ti transmission these calculations showed that ^{43}Sc, an isotope similar in Z and velocity β, is implanted at almost the same depth as ^{44}Ti. Figure 2.6 illustrates the range distribution of ^{44}Ti and ^{43}Sc in the aluminum sample foil based on the momentum distribution selected by the A1200.

The thickness of the Al foils were chosen to implant both, ^{44}Ti and ^{43}Sc, into the sample foil and reduce photon absorbtion in unnecessary material. Also isotopes with a higher Z have a shorter range in Al and might therefore get implanted into the absorber foils. This would reduce the total background activity of the sample. Absorber and veto foils were checked for γ-activity of ^{43}Sc imme-

diately following the implantation to ensure that ^{43}Sc (and therefore also ^{44}Ti) was only implanted into the sample foil (see below in the ^{43}Sc section). Only upper limits were found for absorber ($< 1.6\%$ of the total ^{43}Sc activity) and veto foils ($< 1.2\%$ of the total ^{43}Sc activity), while the sample foil showed significant ^{43}Sc activity.

The total intensity of all ions resulting from the fragmentation on the Be target was monitored continously with two PIN-diodes (Y-monitor and W-monitor) which were installed at the production target. Although these monitors were part of the standard fixed A1200 setup, no information could be found on the exact location of these monitors. Since their absolute count rates were not important for the present experiment it sufficed to know that they were installed at different angles and distances. Two further beam monitors were installed at the target. However, they were severly radiation damaged and not usable. The beam monitor count rates were integrated over 1 minute and then stored to tape on the data aquisistion system. In section 2.3.4 problems with these monitors will be discussed further.

The transmission of the A1200 was checked by remotely replacing the sample with the thin plastic scintillator (T0) every 2 hours for measuring the total number of fragments relative to the beam monitor count rates (see column 14 in Tab. 2.2). It stayed constant within 3.7% over the whole experiment. Since the total rate of fragments would have been too high for the detector and the acquisition computer, the primary beam intensity was reduced by a factor 100.

The ΔE detector, which was inserted at the position of the implantation foil before and after the implantation into each sample, allowed a particle identification from energy loss versus time-of-flight (ΔE vs. TOF) histograms (see Fig.

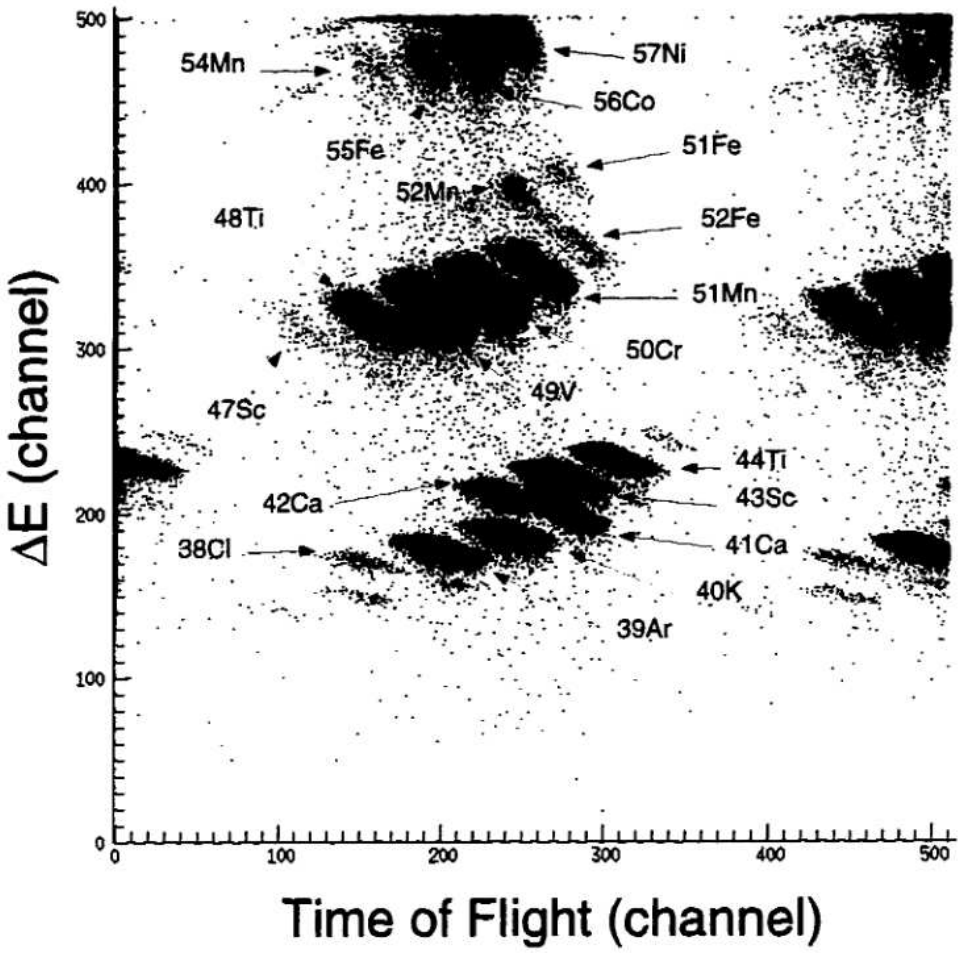

Figure 2.7: ΔE versus time-of-flight histogram as measured by the PIN diode at the sample position.

2.7). Again, the primary beam current was reduced by a factor 100 with respect to the implantation current to limit the count rate. The time-of-flight measurement is started with a signal from the ΔE detector and stopped only by every 2nd RF-pulse from the cyclotron. A detailed discussion on particle identification is given in a section 2.3.3.

Ratios have been formed between each group in the ΔE vs time-of-flight histogram and the total count rate of the Y-monitor. The ratio of the number of

^{44}Ti in the ΔE detector to the Y-monitor count rate, r_{Ti}, stayed constant within 2.3% over the course of the experiment (see column 13 in Tab. 2.2). The number of implanted ^{44}Ti particles could then be determined from the integrated count rate of the Y-monitors and the ratio r_{Ti}, averaged over the 3 measurements:

$$\#Ti = \sum Y_{mon} \cdot r_{Ti} \cdot 2. \tag{2.9}$$

The factor of "2" comes from a specific feature of the time-of-flight measurement which is described in detail in section 2.3.3: each group is duplicated in the ΔE vs time-of-flight histogram because only every second RF-pulse is used to stop the time-of-flight measurement. Table 2.2 shows in detail the parameters to calculate the number of implanted ^{44}Ti particles. The table splits up in measured quantities (left 9 columns) and calculated quantities. All ratios are live time corrected.

Reasons for not using the W-monitor are given in section 2.3.4.

During run 151 a vacuum gate valve closed. A detailed description on how the number of implanted particles is reconstructed is given in the following section. The systematic uncertainty resulting out of this incident must be added linearly to the total number of implanted particles.

During the 20 hours of implantation a total number of $(59.6 \pm 2.6^{+1.6}_{-0.5}) \cdot 10^6$ ^{44}Ti particles was implanted.

Tab. 2.3 shows approximate intensities of all significant ions at the focal plane and some of their decay parameters. The intensities are meant for illustration only, since the primary beam intensity fluctuated during the experiment.

2.3.2 Online method verification with ^{43}Sc

The most prominent radioactive beam contaminant was ^{43}Sc ($t_{1/2}$=3.891h). ^{43}Sc decays by β^+ emission and electron capture to the 372 keV excited state (22.5%)

TABLE 2.2: ^{44}Ti IMPLANTATION MASTER TABLE

Run	Time (hr)	Type	Y-Mon	W-Mon	live (%)	ΔE vs TOF ^{44}Ti	ΔE vs TOF ^{43}Sc	ΔE vs TOF Σ	$\frac{^{43}Sc}{\Sigma}$	$\frac{^{44}Ti}{\Sigma}$	$\frac{^{43}Sc}{Y}$ r_{Sc}	$\frac{^{44}Ti}{Y}$ r_{Ti}
141	0:06	T0	$3.404 \cdot 10^4$	$7.097 \cdot 10^5$	90.2			78927				
142	5:24	#1	$1.447 \cdot 10^8$	$2.356 \cdot 10^9$								
144	0:24	ΔE	$9.298 \cdot 10^4$	$1.932 \cdot 10^6$	89.6	5745	29013	80235	0.362	0.072	0.3484	0.0690
145	0:05	T0	$2.216 \cdot 10^4$	$4.684 \cdot 10^5$	90.4			53803				
146	2:29	#2	$7.317 \cdot 10^7$	$1.173 \cdot 10^9$								
147	0:05	T0	$2.234 \cdot 10^4$	$4.735 \cdot 10^5$	91.0			54944				
148	2:00	#2	$5.337 \cdot 10^7$	$8.736 \cdot 10^8$								
150	0:05	T0	$1.900 \cdot 10^4$	$2.062 \cdot 10^3$	91.9			45999				
151	1:51	#2[a]	$4.182 \cdot 10^7$	$7.076 \cdot 10^8$								
152	0:07	T0	$2.165 \cdot 10^4$	$4.576 \cdot 10^5$	92.9			49987				
153	1:05	#2	$2.495 \cdot 10^7$	$4.221 \cdot 10^8$								
154	0:06	T0	$1.929 \cdot 10^4$	$4.089 \cdot 10^5$	92.7			48431				
155	0:25	ΔE	$8.625 \cdot 10^4$	$1.814 \cdot 10^6$	91.3	5516	28034	76811	0.365	0.072	0.3561	0.0701
156	0:06	T0	$1.778 \cdot 10^4$	$3.774 \cdot 10^5$	93.3			45125				
157	2:32	#3	$5.341 \cdot 10^7$	$9.218 \cdot 10^8$								
158	0:05	T0	$1.470 \cdot 10^4$	$3.101 \cdot 10^5$	93.5			37315				
159	2:07	#3	$4.090 \cdot 10^7$	$7.136 \cdot 10^8$								
160	0:07	T0	$2.272 \cdot 10^4$	$4.733 \cdot 10^5$	93.7			58269				
161	2:08	#3	$3.972 \cdot 10^7$	$6.983 \cdot 10^8$								
162	0:05	T0	$1.578 \cdot 10^4$	$3.320 \cdot 10^5$	94.0			40046				
163	0:18	ΔE	$5.637 \cdot 10^4$	$1.183 \cdot 10^6$	92.0	3475	19483	51524	0.378	0.067	0.3756	0.0670
								Final Value	0.368	0.070	0.3601	0.6869
								Standard Deviation (absolute)	0.005	0.002	0.0140	0.0016
								Relative Uncertainty	1.4%	3.51%	3.90%	2.27%

[a]Vacuum gate valve incident. See text for details.
[b]Best value only. For details see text.
[c]T0 detector only.

TABLE 2.3: FRAGMENT INTENSITIES AT THE A1200 FOCAL PLANE.

Isotope	Intensity [a]	$t_{1/2}$	decay modes [b]
^{44}Ti	640	39 a	EC, β^+, γ 68, 78, 1157
^{43}Sc	3360	3.891 h	β^+, EC, γ 373
^{42}Ca	960	stable	
^{41}Ca	280	$1.03{\cdot}10^5$ a	EC, no γ
^{40}K	1900	$1.2{\cdot}10^9$ a	β^-, β^+, γ 1461
^{39}Ar	1870	269 a	β^-, no γ
^{38}Cl	29	37.2m	β^-, γ 2167, 1624
^{51}Fe	22	0.31s	β^+, γ 749, 320
^{52}Fe	66	8.28h	β^+, γ 169, 744, 936, 1434
^{52}Mn	42	5.591d	EC, β^+, γ 744, 936, 143
^{51}Mn	741	46.2m	EC, β^+, γ 749, 320
^{50}Cr	3470	stable	
^{49}V	3740	337d	EC, no γ
^{48}Ti	730	stable	
^{47}Sc	26	3.35d	β^-, γ 159
^{57}Ni	236	35.6h	EC, β^+, γ 1378, 122, 136
^{56}Co	370	77.3d	EC, β^+, γ 847, 1238
^{55}Fe	142	2.73a	EC, no γ
^{54}Mn	32	312d	EC, γ 835

[a] approximate values only, unit: (s^{-1} pnA^{-1})
[b] including daughter decays

and to the ground state (77.5%) in ^{43}Ca (see Tab. 2.8). The ^{43}Sc ions are very similar in time-of-flight and energy loss to the ^{44}Ti ions, as implied by Figure 2.7 showing both groups close to each other. Due to the short half-life, ^{43}Sc decays partially during the implantaion. Therefore both, the production rate

$$P(t) = 2r_{sc}\frac{dY}{dt} \tag{2.10}$$

and the decay rate λN had to be taken into account. Again, the factor of "2" results from using only every second RF-pulse to stop the time-of-flight measurement. The differential dY/dt represents the count rate of the Y-monitor.

TABLE 2.4: COMPARISON OF THE NUMBER OF IMPLANTED ^{43}Sc WITH THE NUMBER RESULTING FROM THE ACTIVITY MEASUREMENT.

Sample	$N_{impl.}$	A_0(372 keV)	N_{activ} [a]	$\frac{N_{impl.}}{N_{activ}}$ [b]
1	$(65.9 \pm 3.0)\cdot 10^6$	722 ± 34 beq	$(64.8 \pm 3.2)\cdot 10^6$	1.02
2	$(48.3 \pm 2.2)\cdot 10^6$ [c]	528 ± 25 beq	$(47.4 \pm 2.2)\cdot 10^6$	1.02
3	$(53.5 \pm 2.4)\cdot 10^6$	633 ± 30 beq	$(56.9 \pm 2.7)\cdot 10^6$	0.95

[a]Calculated with a half-life of $T_{1/2}$ =3.891h and a branching ratio for the 372 keV emission of f_γ=0.225

[b]The resulting uncertainty is 6.5%.

[c]Best value. Systematic uncertainties range from $46.9\cdot 10^6$ to $52.0\cdot 10^6$ particles.

The number of remaining ^{43}Sc particles in each sample foil at the end of the implantation $N_{Sc}(t_0)$ was calculated by numerically integrating over the differential equation

$$N_{Sc}(t_0) = \int_0^{t_0} [P(t) - \lambda N_{Sc}(t)]\, dt. \qquad (2.11)$$

λ is the decay constant for ^{43}Sc (see Ref. [51]). The fragmented beam was implanted for 5.5, 7.5 and 7 hours into the respective aluminum foil stack. Table 2.4 shows the number of implanted ^{43}Sc particles as calculated.

The foil stacks were removed from the focal plane after the implantation stopped. A 100% HPGe detector (resolution 1.9 keV at 1.33 MeV) was installed on a fixed rail. Lead shielding between 5 and 10cm thickness was built up around the detector. No shielding was put in front of the detector window towards the sample position. The γ-activity of the sample foils was measured at 3 different distances, d = 0.7, 7.3, and 13.3cm from the active region of the germanium detector crystal. The activity A can be determined from the count rate in the respective γ-ray peak, N_i/t, the peak efficiency at the respective energy, ϵ^P, the branching ratio f_i, a photon absorption correction factor C_{abs}, and a summing

correction factor C_{sum} (as defined in section 2.3.5.3):

$$A = \frac{N_i}{\epsilon^P f_i t} C_{abs} C_{sum} \tag{2.12}$$

Corrections for coincidence summing between the the 372 keV emission and the positron annihilation photons have been calculated. Only at $d = 0.7$cm did coincidence summing contribute significantly. The total efficiency for one 511 keV photon, ϵ^T_{511}, was calculated using the method described in section 2.3.5.3. With a calculated value $\epsilon^T_{511} = 30 \pm 2\%$ and using equation 2.17 the correction factor for summing comes to

$$C_{sum} = 1.87 \pm 0.08, \tag{2.13}$$

where the quoted error reflects a systematic uncertainty of the calculation due to the geometry of the detector source setup.

The peak efficiencies, ϵ^P, at the respective distances were measured using the γ-ray emissions at 248, 428, and 463 keV of a calibrated ^{154}Eu, ^{125}Sb mixed source. Summing corrections for the calibration source were calculated according to the cascade information in the reference sheet of the source [52] and with the method described in Ref. [53] using the photon interaction cross sections from Ref. [54] (see also section 2.3.5.3). The correction factors for ϵ^P_i at $d = 0.7$cm are

$$\begin{aligned} C_{sum}(248keV) &= 1.50, \\ C_{sum}(428keV) &= 1.004, \\ C_{sum}(463keV) &= 1.07, \end{aligned} \tag{2.14}$$

with a systematic uncertainty of 4%.

For the summing corrections of the calibration source it is necessary to calculate ϵ^T for many γ-ray energies (see Ref. [52]). The absorption in the aluminum window of the detector of low energy gammas (27, 36, and 43 keV) emitted by the calibration source influences the respective efficiency significantly and were calculated using the same cross section tables [54]. The absorption correction C_{abs} is more accurately defined as the number of incident photons divided by the number of photons passing through the absorber. Therefore

$$C_{abs} = e^{\mu x}, \tag{2.15}$$

where μ is the total absorbtion cross section from Ref. [54], and x the average distance through the material. Strong absorption of these lines is to be expected: $C_{abs} = 6.67$. This factor has already been included in the summing correction terms in Eq. 2.14.

Pile-up occurs, when two or more uncorrelated events arrive "simultaneously" in the detector. Simultaneous events are those which occur within a fraction of the amplifier shaping time (3μs in our case), without significantly disturbing the shape of the pre-amplified signal. Pile-up is therefore a rate dependent effect. One can introduce pulser generated pulses into the pre-amplifier test input. With the assumption that pile-up occurs between real signals (e.g. photons) as well as between photons and the pulser signals, at equal rate, one can measure the effect of pile-up and dead time simultaneously by comparing the generated pulses with the number of detected pulses. In the present experiment we generated pulses at a frequency of 10Hz. The pulse height was chosen to be at the upper end of the spectrum to avoid overlap with the peaks of interest. For a detailed discussion on pile-up rejection see Ref. [55] Significant pile-up occured only during the

efficiency calibration at $d = 0.7$cm.

The measured half-life from the slope of the (logarithmic) decay curve ($t_{1/2} = 3.88 \pm 0.05$h) is in excellent agreement with the well known half-life of ^{43}Sc ($t_{1/2} = 3.891 \pm 0.012$ h [51]). The initial ^{43}Sc activity was determined by extrapolation of the decay curve to the time when implantation was stopped. Table 2.4 shows the results of this extrapolation and Figure 2.8 shows the decay curve for the activity measurement of the first sample. Since the individual data points on the decay curve have been measured at different distances d, the figure also demonstrates that summing and pile-up corrections have been applied correctly. The uncertainty of the initial activity is 1.8% due to the fit plus 4.3% due to the absolute efficiency, yielding a total uncertainty of 4.7% for the first sample. For the first and third implanted sample this procedure gave an independent method to determine the number of implanted ^{43}Sc particles. Both numbers agree well within the quoted uncertainties (see Tab. 2.4). These results suggest that the employed implantation technique will also work reliably for ^{44}Ti within similar uncertainties.

During the implantation of the fragmented beam into the second sample a vacuum gate valve at the focal plane closed unnoticed between two transmission checks (run 151 in Tab. 2.2). Particles were still produced and counted by the beam monitors, but not necessarily implanted into the sample for a time period of 111 minutes. Using sample 1 and 3 as a calibration for $N_{impl.}/N_{activ}$ in Tab. 2.4 the number of implanted ^{43}Sc particles in sample 2 can be reconstructed by numerically integrating Eq. 2.11 and variing the time t_{GV} after which $P(t > t_{GV}) = 0$. The best value for the time t_{GV} of the gate valve closing was determined to be 9 minutes after the start of the run: $N_{impl.}/N_{activ}$=1.02 at

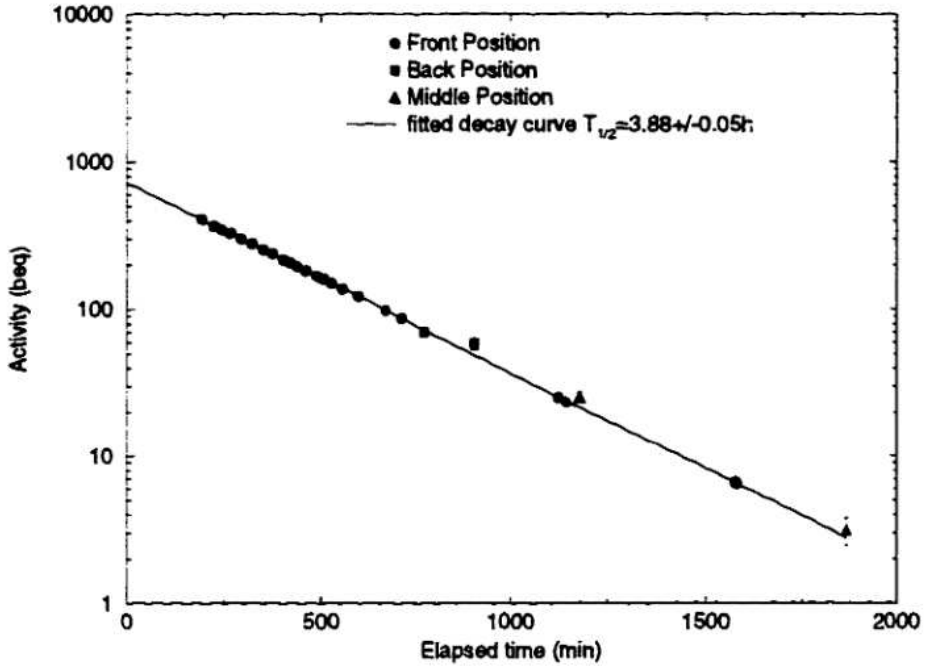

Figure 2.8: The measured ^{43}Sc decay curve of the first sample. Some symbol sizes exceed the error bars. The activity was measured at three different distances.

t_{GV} =9 minutes in excellent agreement with the other two values (Tab. 2.4). Beam monitor fluctuations indicate something that could have been a spark after 9 minutes. A spark could have caused the vacuum interlock to react and close the valve. However, within the 1σ uncertainties of the $N_{impl.}/N_{activ}$ ratio (6.5%) values for t_{GV} between 0 and 41 minutes are consistent. We therefore add this systematic error separately from the statistical error to the total number of implanted ^{44}Ti particles and determine therefore a total number of $(59.6 \pm 2.6^{+1.6}_{-0.5}) \cdot 10^6$ ^{44}Ti particles.

2.3.3 Particle identification

In order to ensure that no ^{44}Ti or ^{43}Sc in a different charge state has been neglected all groups in the ΔE vs Time of Flight histogram (Fig. 2.7) have

been identified. To further reduce the possibility of systematic uncertainties all γ-emitting decays in our sample have been investigated and compared to the number of implanted particles of the respective isotope or its parent isotopes.

Using the computer code INTENSITY [50] fragment transmission parameters have been calculated. With $B\rho_1 = 2.1477$ and $B\rho_3 = 1.8477$, the magnetic rigidities for both dipole elements of the A1200, kept constant, the thickness of the production target has been varied within its uncertainties. This yields a complete set of fragments that could have arrived at the focal plane, pending their actual intensities due to fragmentation cross section and angular acceptance parameters. Fragments were produced in different charge states. Passing through the degrader-wedge some fragments picked up an electron. For the time-of-flight calculation both charge states, before and after the wedge, have to be known, so that one can accurately determine the (relativistic) velocities β_w and β_{out}, before the wedge and after the wedge, respectively. The computer code INTENSITY also calculates the position of each fragment in the focal plane. The ΔE-detector as well as the sample had a width of 5cm which was taken into account for the intensity calculations. Table 2.5 summarizes the results of these calculations.

Ranges of each fragment in Al were computed with the code LISE, comparing fragment energies to the ones calculated with INTENSITY. The ranges were compared to absorber, sample and veto foil thicknesses. Figure 2.9 shows the ranges of relevant isotopes in the sample foil. No ions were stopped in the absorber foil; none passed through the sample into the veto, according to the calculations.

In an attempt to verify the position of ^{54}Mn, a high-Z, long lived isotope, an activity measurement of all foils of all stacks has been started 833 days after

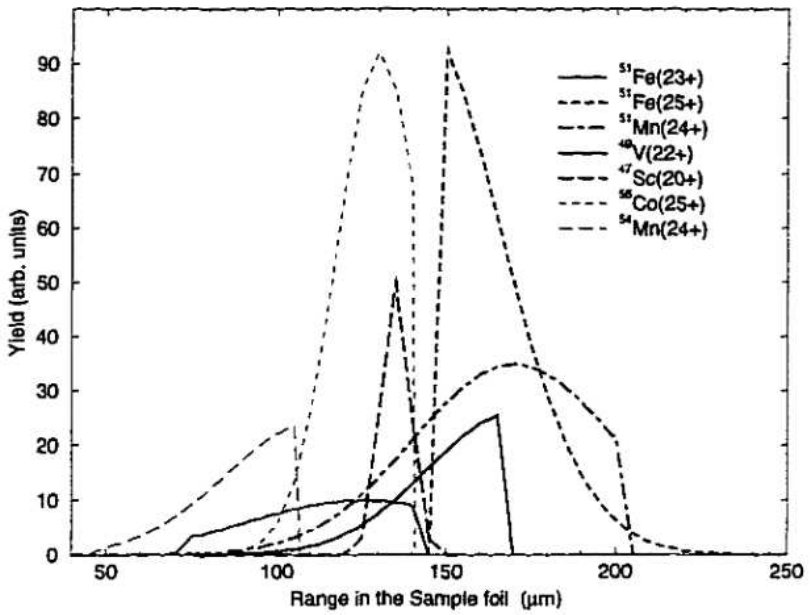

Figure 2.9: Ranges of relevant ions in the sample foil. Bold lines indicate isotopes in the middle band, light lines in the upper band of Fig. 2.7.

implantation stop. Within the uncertainty of 8% the resulting activity is identical with the one from the sample only. This confirms that all ^{54}Mn has in fact been implanted into the sample rather than in the absorber. Other isotopes had decayed beyond detection limits at this point.

At the focal plane of the A1200 energy loss of the fragments was measured with a 500 μm thick Si-detector. The detector was calibrated with the degrader removed from the A1200, identifying particles by counting the groups in the ΔE vs time-of-flight histogram starting at ^{8}Be, a hole in the $N = Z$ line of isotopes. Energy loss calculations have been performed with the computer code ATIMA03 [56] for all fragments. The program ATIMA03 is explained in the Appendix. Table 2.5 shows the results of the calculations for all relevant fragments.

For the time-of-flight calibration several facts have to be considered. The

velocities are different for the flight path before and after the wedge (14.5m and 8m, respectively). A signal in the ΔE detector started the time measurement and a RF-pulse stopped the measurement. With the cyclotron RF-pulse interval of 55ns, only every second RF-pulse was used as a possible stop pulse, in order to account for the spread in flight times for different isotopes of interest. The RF-pulse provides slope information for the time-of-flight calibration: Depending on which pulse produces the ions that generate the start pulse in the ΔE-detector, one of two equally probable pulses will stop the time measurement. This effect can be seen in the time-of-flight histogram by the apparent wrap-around of some groups. All groups wrap, however the selected time window allows only a few groups to appear in the histogram. The time difference between two wrapped groups is the interval between two pulses, 55ns.

At the time of the experiment the isotopes of interest were only the ones in the lowest band of Fig. 2.7 and little attention was paid to slower ions, mainly found in the upper band of Fig. 2.7. It turns out that some of these ions are slow enough to arrive at the ΔE-detector after the stop pulse for the fastest ions. These slow ions create their own start signal. The respective stop RF-pulse is then of course a different one and a different calibration has to be used to calculate the time-of-flight for these ions from the time-of-flight histogram. One cannot conclude from the histogram directly which groups are affected. We therefore calculated the time-of-flight for all ions and compared our results with different calibrations which are offset by one RF-cycle, with respect to each other. It turns out that most of the upper band and a few middle band groups have been shifted this way and can be found much further to the right in Fig 2.7 than expected with a linear calibration.